Supplement to "The Biogeophysical Effects of Carbon Fertilization of the Terrestrial Biosphere"

Robert J. Allen[1*]

[1]Department of Earth and Planetary Sciences, University of California, Riverside USA

[*]corresponding author email: rjallen@ucr.edu

Contents:

Supplementary Information

Supplementary Note 1: Additional Investigation of Model Differences

As discussed in the main text, models with a terrestrial nitrogen cycle (N models; Supplementary Table 1) yield smaller increases in land carbon storage, and to some extent weaker increases in NPP and LAI, as compared to models without a terrestrial nitrogen cycle (noN models). Although most of these differences are not significant between these two model subsets, I investigate further. Interestingly, N models also tend to yield larger biogeophysical warming (but not significantly so). For example, the global mean TAS response is 0.23 ± 0.11 K in the eight N models versus 0.08 ± 0.15 K in the six noN models. Similar results occur over global land only at 0.38 ± 0.17 K versus 0.16 ± 0.20 K, resepectively. To some extent this seems counterintuitive since the 15 model mean yields warming in response to the increase vegetation, and one might expect models with a larger vegetation increase to yield more biogeophysical warming. However, intermodel correlations between the vegetation responses and the land TAS response are not significant at -0.03 for LAI; -0.03 for NPP; and -0.34 for land carbon. Thus, intermodel differences in biogeophysical warming are not well correlated with intermodel differences in vegetation indices.

Consistently, the intermodel correlation between the total SEB response (i.e. biogeophysical warming) and biogeochemical cooling displays a (non-significant) positive correlation at 0.34. This correlation is identical to that above based on land carbon storage (but positive here), which is a direct consequence of inferring biogeochemical cooling from the best estimate of the TCRE and each model's land carbon response. This again implies that models that yield weaker biogeochemical cooling also tend to yield more biogeophysical warming (i.e., N models) and vice versa. In other words, N cycle models would yield less overall cooling under carbon fertilization, due to both less biogeochemical cooling associated with less carbon storage but more warming associated with biogeophysical effects. This result does not appear to the related to differences in TCR, as models with a terrestrial nitrogen cycle yield a TCR of 2.1 ± 0.20 K whereas models without a terrestrial nitrogen cycle yield a TCR of 1.9 ± 0.31 K.

I note that most of the land warming differences between N models and noN models occurs over extratropical land at 0.49 ± 0.22 K versus 0.16 ± 0.26 K, respectively. As with the global land intermodel correlations, however, there are no significant correlations between extratropical land warming and extratropical vegetation indices at -0.14 for LAI; -0.38 for NPP; and -0.38 for land carbon. Nonetheless, each extratropical SEB term response for the N models is larger in magnitude (some more positive and some more negative) as compared to the noN models. The largest extratropical difference between these two model subsets is for the SEB albedo term (0.22 ± 0.14 K in the N models 0.11 ± 0.13 K in the noN models) and for the SEB SW term (0.21 ± 0.16 K in the N models versus 0.11 ± 0.10 K in the noN models). Most of the larger increase in the extratropical SEB SW term in the N models is due to SW_{cloud} at 0.27 ± 0.12 K versus 0.14 ± 0.09 K in the noN models. I note relatively small differences in the extratropical LH SEB term at 0.21 ± 0.21 K in the N models versus 0.16 ± 0.15 K in the noN models. The extratropical SEB LH response in the N models has both larger warming due to the SEB transpiration term but also larger cooling due to the SEB evaporation term. For example, the former term is 0.52 ± 0.19 K and the latter term is -0.35 ± 0.18 K in the N models. The corresponding responses for the noN models are 0.16 ± 0.08 K versus -0.001 ± 0.16 K. Similar statements for the global and tropical mean SEB LH, transpiration and evaporation terms exist. Thus, the enhanced biogeophysical warming in N models—most of which occurs in the extratropics—does not appear to be driven by LH differences, and is instead related to both the SEB albedo and SW_{cloud} terms. In addition to terrestrial nitrogen cycling, these two model subsets share many other differences (e.g., photosynthesis, stomatal conductance, litter/soil carbon dynamics, etc.) that likely complicate a simple interpretation.

Supplementary References

Boucher, O., Servonnat, J., Albright, A. L., Aumont, O., Balkanski, Y., Bastrikov, V., Bekki, S., Bonnet, R., Bony, S., Bopp, L., Braconnot, P., Brockmann, P., Cadule, P., Caubel, A., Cheruy, F., Codron, F., Cozic, A., Cugnet, D., D'Andrea, F., Davini, P., de Lavergne, C., Denvil, S., Deshayes, J., Devilliers, M., Ducharne, A., Dufresne, J.-L., Dupont, E., Éthé, C., Fairhead, L., Falletti, L., Flavoni, S., Foujols, M.-A., Gardoll, S., Gastineau, G., Ghattas, J., Grandpeix, J.-Y., Guenet, B., Guez, Lionel, E., Guilyardi, E., Guimberteau, M., Hauglustaine, D., Hourdin, F., Idelkadi, A., Joussaume, S., Kageyama, M., Khodri, M., Krinner, G., Lebas, N., Levavasseur, G., Lévy, C., Li, L., Lott, F., Lurton, T., Luyssaert, S., Madec, G., Madeleine, J.-B., Maignan, F., Marchand, M., Marti, O., Mellul, L., Meurdesoif, Y., Mignot, J., Musat, I., Ottlé, C., Peylin, P., Planton, Y., Polcher, J., Rio, C., Rochetin, N., Rousset, C., Sepulchre, P., Sima, A., Swingedouw, D., Thiéblemont, R., Traore, A. K., Vancoppenolle, M., Vial, J., Vialard, J., Viovy, N., and Vuichard, N.: Presentation and Evaluation of the IPSL-CM6A-LR Climate Model, J. Adv. Model. Earth Sy., 12, e2019MS002010, https://doi.org/10.1029/2019MS002010, 2020.

Danabasoglu, G., Lamarque, J.-F., Bacmeister, J., Bailey, D. A., DuVivier, A. K., Edwards, J., Emmons, L. K., Fasullo, J., Garcia, R., Gettelman, A., Hannay, C., Holland, M. M., Large, W. G., Lauritzen, P. H., Lawrence, D. M., Lenaerts, J. T. M., Lindsay, K., Lipscomb, W. H., Mills, M. J., Neale, R., Oleson, K. W., Otto-Bliesner, B., Phillips, A. S., Sacks, W., Tilmes, S., van Kampenhout, L., Vertenstein, M., Bertini, A., Dennis, J., Deser, C., Fischer, C., Fox-Kemper, B., Kay, J. E., Kinnison, D., Kushner, P. J., Larson, V. E., Long, M. C., Mickelson, S., Moore, J. K., Nienhouse, E., Polvani, L., Rasch, P. J., and Strand, W. G.: The Community Earth System Model Version 2 (CESM2), J. Adv. Model. Earth Sy., 12, e2019MS001916, https://doi.org/10.1029/2019ms001916, 2020.

Döscher, R., Acosta, M., Alessandri, A., Anthoni, P., Arsouze, T., Bergman, T., Bernardello, R., Boussetta, S., Caron, L.-P., Carver, G., Castrillo, M., Catalano, F., Cvijanovic, I., Davini, P., Dekker, E., Doblas-Reyes, F. J., Docquier, D., Echevarria, P., Fladrich, U., Fuentes-Franco, R., Gröger, M., v. Hardenberg, J., Hieronymus, J., Karami, M. P., Keskinen, J.-P., Koenigk, T., Makkonen, R., Massonnet, F., Ménégoz, M., Miller, P. A., Moreno-Chamarro, E., Nieradzik, L., van Noije, T., Nolan, P., O'Donnell, D., Ollinaho, P., van den Oord, G., Ortega, P., Prims, O. T., Ramos, A., Reerink, T., Rousset, C., Ruprich-Robert, Y., Le Sager, P., Schmith, T., Schrödner, R., Serva, F., Sicardi, V., Sloth Madsen, M., Smith, B., Tian, T., Tourigny, E., Uotila, P., Vancoppenolle, M., Wang, S., Wårlind, D., Willén, U., Wyser, K., Yang, S., Yepes-Arbós, X., and Zhang, Q.: The EC-Earth3 Earth system model for the Coupled Model Intercomparison Project 6, Geosci. Model Dev., 15, 2973–3020, https://doi.org/10.5194/gmd-15-2973-2022, 2022.

Dunne, J. P., Horowitz, L. W., Adcroft, A. J., Ginoux, P., Held, I. M., John, J. G., Krasting, J. P., Malyshev, S., Naik, V., Paulot, F., Shevliakova, E., Stock, C. A., Zadeh, N., Balaji, V., Blanton, C., Dunne, K. A., Dupuis, C., Durachta, J., Dussin, R., Gauthier, P. P. G., Griffies, S. M., Guo, H., Hallberg, R. W., Harrison, M., He, J., Hurlin, W., McHugh, C., Menzel, R., Milly, P. C. D., Nikonov, S., Paynter, D. J., Ploshay, J., Radhakrishnan, A., Rand, K., Reichl, B. G., Robinson, T., Schwarzkopf, D. M., Sentman, L. T., Underwood, S., Vahlenkamp, H., Winton, M., Wittenberg, A. T., Wyman, B., Zeng, Y., and Zhao, M.: The GFDL Earth System Model Version 4.1 (GFDL-ESM 4.1): Overall Coupled Model Description and Simulation Characteristics, J. Adv. Model. Earth Sy., 12, e2019MS002015, https://doi.org/10.1029/2019ms002015, 2020.

Kelley, M., Schmidt, G. A., Nazarenko, L. S., Bauer, S. E., Ruedy, R., & Russell, G. L., et al. GISS-E2.1: Configurations and climatology. *Journal of Advances in Modeling Earth Systems*, 12, e2019MS002025, https://doi.org/10.1029/2019MS002025, 2020.

Law, R. M., Ziehn, T., Matear, R. J., Lenton, A., Chamberlain, M. A., Stevens, L. E., Wang, Y. P., Srbinovsky, J., Bi, D., Yan, H., and Vohralik, P. F.: The carbon cycle in the Australian Community Climate and Earth System Simulator (ACCESS-ESM1) – Part 1: Model description and pre-industrial simulation, Geosci. Model Dev., 10, 2567–2590, https://doi.org/10.5194/gmd-10-2567-2017, 2017.

Lovato, T., Peano, D., Butenschon, M., Materia, S., Iovino, D., Scoccimarro, E., Fogli, P. G., Cherchi, A., Bellucci, A., Gualdi, S., Masina, S., and Navarra, A.: CMIP6 Simulations With the CMCC Earth System Model (CMCC-ESM2), J. Adv. Model. Earth Sy., 14, e2021MS002814, https://doi.org/10.1029/2021MS002814, 2022.

Mauritsen, T., Bader, J., Becker, T., Behrens, J., Bittner, M., Brokopf, R., Brovkin, V., Claussen, M., Crueger, T., Esch, M., Fast, I., Fiedler, S., Fläschner, D., Gayler, V., Giorgetta, M., Goll, D. S., Haak, H., Hagemann, S., Hedemann, C., Hohenegger, C., Ilyina, T., Jahns, T., Jimenéz-de-la Cuesta, D., Jungclaus, J., Kleinen, T., Kloster, S., Kracher, D., Kinne, S., Kleberg, D., Lasslop, G., Kornblueh, L., Marotzke, J., Matei, D., Meraner, K., Mikolajewicz, U., Modali, K., Möbis, B., Müller, W. A., Nabel, J. E. M. S., Nam, C. C. W., Notz, D., Nyawira, S.-S., Paulsen, H., Peters, K., Pincus, R., Pohlmann, H., Pongratz, J., Popp, M., Raddatz, T. J., Rast, S., Redler, R., Reick, C. H., Rohrschneider, T., Schemann, V., Schmidt, H., Schnur, R., Schulzweida, U., Six, K. D., Stein, L., Stemmler, I., Stevens, B., von Storch, J.-S., Tian, F., Voigt, A., Vrese, P., Wieners, K.-H., Wilkenskjeld, S., Winkler, A., and Roeckner, E.: Developments in the MPI-M Earth System Model version 1.2 (MPI-ESM1.2) and Its Response to Increasing CO2, J. Adv. Model. Earth Sy., 11, 998–1038, https://doi.org/10.1029/2018ms001400, 2019.

Séférian, R., Nabat, P., Michou, M., Saint-Martin, D., Voldoire, A., Colin, J., Decharme, B., Delire, C., Berthet, S., Chevallier, M., Sénési, S., Franchisteguy, L., Vial, J., Mallet, M., Joetzjer, E., Geoffroy, O., Guérémy, J.-F., Moine, M.-P., Msadek, R., Ribes, A., Rocher, M., Roehrig, R., Salas-y Mélia, D., Sanchez, E., Terray, L., Valcke, S., Waldman, R., Aumont, O., Bopp, L., Deshayes, J., Éthé, C., and Madec, G.: Evaluation of CNRM Earth System Model, CNRM-ESM2-1: Role of Earth System Processes in Present-Day and Future Climate, J. Adv. Model. Earth Sy., 11, 4182–4227, https://doi.org/10.1029/2019MS001791, 2019.

Seland, Ø., Bentsen, M., Olivié, D., Toniazzo, T., Gjermundsen, A., Graff, L. S., Debernard, J. B., Gupta, A. K., He, Y.-C., Kirkevåg, A., Schwinger, J., Tjiputra, J., Aas, K. S., Bethke, I., Fan, Y., Griesfeller, J., Grini, A., Guo, C., Ilicak, M., Karset, I. H. H., Landgren, O., Liakka, J., Moseid, K. O., Nummelin, A., Spensberger, C., Tang, H., Zhang, Z., Heinze, C., Iversen, T., and

Schulz, M.: Overview of the Norwegian Earth System Model (NorESM2) and key climate response of CMIP6 DECK, historical, and scenario simulations, Geosci. Model Dev., 13, 6165–6200, https://doi.org/10.5194/gmd-13-6165-2020, 2020.

Sellar, A. A., Jones, C. G., Mulcahy, J. P., Tang, Y., Yool, A., Wiltshire, A., O'Connor, F. M., Stringer, M., Hill, R., Palmieri, J., Woodward, S., de Mora, L., Kuhlbrodt, T., Rumbold, S. T., Kelley, D. I., Ellis, R., Johnson, C. E., Walton, J., Abraham, N. L., Andrews, M. B., Andrews, T., Archibald, A. T., Berthou, S., Burke, E., Blockley, E., Carslaw, K., Dalvi, M., Edwards, J., Folberth, G. A., Gedney, N., Griffiths, P. T., Harper, A. B., Hendry, M. A., Hewitt, A. J., Johnson, B., Jones, A., Jones, C. D., Keeble, J., Liddicoat, S., Morgenstern, O., Parker, R. J., Predoi, V., Robertson, E., Siahaan, A., Smith, R. S., Swaminathan, R., Woodhouse, M. T., Zeng, G., and Zerroukat, M.: UKESM1: Description and Evaluation of the UK Earth System Model, J. Adv. Model. Earth Sy., 11, 4513–4558, https://doi.org/10.1029/2019MS001739, 2019.

Swart, N. C., Cole, J. N. S., Kharin, V. V., Lazare, M., Scinocca, J. F., Gillett, N. P., Anstey, J., Arora, V., Christian, J. R., Hanna, S., Jiao, Y., Lee, W. G., Majaess, F., Saenko, O. A., Seiler, C., Seinen, C., Shao, A., Sigmond, M., Solheim, L., von Salzen, K., Yang, D., and Winter, B.: The Canadian Earth System Model version 5 (CanESM5.0.3), Geosci. Model Dev., 12, 4823–4873, https://doi.org/10.5194/gmd-12-4823-2019, 2019.

Wu, T., Lu, Y., Fang, Y., Xin, X., Li, L., Li, W., Jie, W., Zhang, J., Liu, Y., Zhang, L., Zhang, F., Zhang, Y., Wu, F., Li, J., Chu, M., Wang, Z., Shi, X., Liu, X., Wei, M., Huang, A., Zhang, Y., and Liu, X.: The Beijing Climate Center Climate System Model (BCC-CSM): the main progress from CMIP5 to CMIP6 , Geosci. Model Dev., 12, 1573–1600, https://doi.org/10.5194/gmd-12-1573-2019, 2019.

Yukimoto, S., Kawai, H., Koshiro, T., Oshima, N., Yoshida, K., Urakawa, S., Tsujino, H., Deushi, M., Tanaka, T., Hosaka, M., Yabu, S., Yoshimura, H., Shindo, E., Mizuta, R., Obata, A., Adachi, Y., and Ishii, M.: The Meteorological Research Institute Earth System Model Version 2.0, MRI-ESM2.0: Description and Basic Evaluation of the Physical Component, J. Meteorol. Soc. Jpn. Ser. II, 97, 931–965, https://doi.org/10.2151/jmsj.2019-051, 2019.

Ziehn, T., Chamberlain, M. A., Law, R. M., Lenton, A., Bodman, R. W., Dix, M., Stevens, L., Wang, Y.-P., and Srbinovsky, J.: The Australian Earth System Model: ACCESS-ESM1.5, J. Southern Hemisph. Earth Syst. Sci., 70, 193–214, https://doi.org/10.1071/es19035, 2020.

Supplementary Table 1. CMIP6 models analyzed here. In the comment section, D represents models with a dynamic global vegetation model (i.e., vegetation type and distribution are interactive); N represents models that include a terrestrial nitrogen cycle; and C represents models that include atmospheric chemistry with interactive BVOC emissions.

Model	Atmosphere Model	Land Model	Comment	Main Reference
ACCESS-ESM1-5	UM7.3	CABLE2.4, CASA-CNP	N	Law et al. (2017), Ziehn et al. (2020)
BCC-CSM2-MR	BCC AGCM3 MR	BCC AVIM2		Wu et al. (2019)
CanESM5	CanAM5	CLASS3.6, CTEM1.2		Swart et al. (2019)
CESM2	CAM6	CLM5	N	Danabasoglu et al. (2020)
CMCC-ESM2	CAM5	CLM4.5	N	Lovato et al. (2022)
CNRM-ESM2-1	ARPEGE-Climate v6.3 + SURFEX v8.0	ISBA + CTRIP		Seferian et al. (2019)
EC-Earth3-CC	IFS 36r4 + HTESSEL + TM5	LPJ-GUESS	N	Doscher et al. (2022)
GISS-E2-1-G	GISS-E2.1	GISS LSM		Kelley et al. (2020)
GFDL-ESM4	AM4.1	LM4.1	D, C	Dunne et al. (2020)
IPSL-CM6A-LR	LMDZ6A	ORCHIDEEv2		Boucher et al. (2020)
MIROC-ES2L	MIROC-AGCM + SPRINTARS	VISIT-e and MATSIRO6	N	Hajima et al. (2020)
MPI-ESM1-2-LR	ECHAM6.3	JSBACH3.2	N, D	Mauritsen et al. (2019)
MRI-ESM2-0	MRI-AGCM3.5 + MASINGAR mk-2r4c + MRI-CCM2.1	HAL		Yukimoto et al. (2019)
NorESM2-LM	Modified CAM6	CLM5	N, C	Seland et al. (2020)
UKESM1-0-LL	Unified Model + UKCA	JULES-ES-1.0	N, D, C	Sellar et al. (2019)

Supplementary Table 2. Vegetation and land carbon responses associated with carbon fertilization. Global, tropical and extratropical multimodel mean annual mean responses for net primary productivity (NPP; kg km^{-2} day^{-1}]; leaf area index (LAI; dimensionless); litter carbon (cLitter; kgC m^{-2}); soil organic matter carbon (cSoil; kgC m^{-2}); vegetation carbon (cVegetation; kgC m^{-2}); and land carbon (cLand; kgC m^{-2}). Uncertainty represents the 90% confidence interval estimated as $\frac{1.65\times\sigma}{\sqrt{m}}$, where σ is the standard deviation across models and *m* is the number of models. Responses not significant at the 90% confidence level are in bold.

	Global		**Tropics**		**Extratropics**	
	MMM	**# Models**	**MMM**	**# Models**	**MMM**	**# Models**
NPP	679.4 ± 140.6	15/15	1049.7 ± 248.2	15/15	516.7 ± 109.4	15/15
LAI	0.71 ± 0.25	14/15	1.12 ± 0.41	14/15	0.52 ± 0.18	14/15
cLitter	0.66 ± 0.22	13/13	0.70 ± 0.26	13/13	0.77 ± 0.28	13/13
cSoil	1.38 ± 0.49	14/14	1.68 ± 0.64	14/14	1.49 ± 0.57	14/14
cVegetation	2.48 ± 0.42	14/14	3.97 ± 0.68	14/14	1.76 ± 0.47	14/14
cLand	4.52 ± 0.68	14/14	6.35 ± 0.97	14/14	4.02 ± 0.79	14/14

Supplementary Table 3. Climate responses associated with carbon fertilization. Global, tropical and extratropical multimodel mean annual mean responses for near-surface air temperature (TAS; K); TAS over land (TAS LND; K); surface temperature (TS; K); TS over land (TS LND; K); precipitation (PR; mm day^{-1}); PR over land (PR LND; mm day^{-1}); near-surface wind speed (WS; m s^{-1}); WS over land (WS LND; m s^{-1}); total cloud cover (CLT; %); CLT over land (CLT LND; %); tropospheric specific humidity (TQ; g kg^{-1}); TQ over land (TQ LND; g kg^{-1}); tropospheric relative humidity (TRH; %); TRH over land (TRH LND; %); tropospheric temperature (TTEMP; K); TTEMP over land (TTEMP LND; K); near-surface specific humidity (QS; g kg^{-1}); QS over land (QS LND; g kg^{-1}); near-surface relative humidity (RHS; %); RHS over land (RHS LND; %); aerosol optical depth (AOD; 10^{-3}); AOD over land (AOD LND; 10^{-3}); dust aerosol optical depth (DAOD; 10^{-3}); DAOD over land (DAOD LND; 10^{-3}); aerosol optical depth without dust (AODNOD; 10^{-3}); and AODNOD over land (AODNOD LND; 10^{-3}). Uncertainty represents the 90% confidence interval estimated as $\frac{1.65\times\sigma}{\sqrt{m}}$, where σ is the standard deviation across models and *m* is the number of models. Responses not significant at the 90% confidence level are in bold.

	Global		**Tropics**		**Extratropics**	
	MMM	**# Models**	**MMM**	**# Models**	**MMM**	**# Models**
TAS	0.16 ± 0.09	13/15	0.13 ± 0.05	13/15	0.18 ± 0.10	13/15
TAS LND	0.28 ± 0.13	14/15	0.25 ± 0.09	14/15	0.33 ± 0.17	14/15
TS	0.15 ± 0.09	13/15	0.12 ± 0.05	13/15	0.16 ± 0.10	13/15
TS LND	0.26 ± 0.12	13/15	0.22 ± 0.09	13/15	0.31 ± 0.16	14/15
PR	-0.012 ± 0.009	11/15	-0.021 ± 0.009	13/15	$\mathbf{-0.008 \pm 0.009}$	11/15
PR LND	-0.028 ± 0.017	12/15	-0.038 ± 0.023	12/15	-0.032 ± 0.020	13/15
WS	-0.013 ± 0.009	10/15	$\mathbf{-0.011 \pm 0.011}$	9/15	-0.022 ± 0.010	11/15
WS LND	-0.040 ± 0.023	9/15	$\mathbf{-0.025 \pm 0.030}$	9/15	-0.069 ± 0.029	12/15
CLT	-0.22 ± 0.09	12/15	-0.20 ± 0.09	12/15	-0.31 ± 0.12	14/15
CLT LND	-0.52 ± 0.23	12/15	-0.56 ± 0.28	12/15	-0.64 ± 0.29	12/15
TQ	0.017 ± 0.014	11/15	0.022 ± 0.019	11/15	0.014 ± 0.011	11/15
TQ LND	$\mathbf{0.011 \pm 0.015}$	10/15	$\mathbf{0.012 \pm 0.019}$	8/15	$\mathbf{0.012 \pm 0.015}$	9/15
TRH	-0.09 ± 0.05	12/14	-0.11 ± 0.05	11/14	-0.11 ± 0.06	13/14
TRH LND	-0.21 ± 0.12	12/14	-0.26 ± 0.14	12/14	-0.27 ± 0.17	12/14
TTEMP	0.14 ± 0.08	13/15	0.13 ± 0.08	11/15	0.15 ± 0.07	14/15

TTEMP LND	0.18 ± 0.09	14/15	0.17 ± 0.08	14/15	0.21 ± 0.09	14/15
QS	$\mathbf{0.041 \pm 0.042}$	11/15	$\mathbf{0.049 \pm 0.054}$	10/15	0.037 ± 0.035	11/15
QS LND	$\mathbf{-0.010 \pm 0.052}$	9/15	$\mathbf{-0.033 \pm 0.072}$	9/15	$\mathbf{0.003 \pm 0.049}$	9/15
RHS	-0.27 ± 0.16	11/14	-0.29 ± 0.17	11/14	-0.27 ± 0.17	11/14
RHS LND	-0.87 ± 0.48	11/14	-1.09 ± 0.59	11/14	-0.92 ± 0.57	11/14
AOD	$\mathbf{1.11 \pm 1.13}$	5/8	$\mathbf{1.32 \pm 1.43}$	5/8	$\mathbf{1.02 \pm 1.21}$	3/8
AOD LND	$\mathbf{1.88 \pm 2.50}$	5/8	3.07 ± 3.00	5/8	$\mathbf{1.23 \pm 3.38}$	3/8
DAOD	$\mathbf{0.34 \pm 0.76}$	5/8	$\mathbf{0.41 \pm 0.87}$	4/8	$\mathbf{0.29 \pm 1.11}$	4/8
DAOD LND	$\mathbf{0.40 \pm 1.60}$	5/8	$\mathbf{0.72 \pm 1.80}$	5/8	$\mathbf{0.14 \pm 2.81}$	4/8
AODNOD	$\mathbf{0.77 \pm 0.86}$	4/8	$\mathbf{0.91 \pm 1.03}$	5/8	$\mathbf{0.73 \pm 0.89}$	6/8
AODNOD LND	$\mathbf{1.49 \pm 1.71}$	5/8	2.35 ± 2.33	5/8	$\mathbf{1.10 \pm 1.75}$	4/8

Supplementary Table 4. Surface energy balance (SEB) decomposition of the surface temperature response. Global, tropical and extratropical multimodel mean annual mean responses and the number of models that agree on the sign of the multimodel mean response. Terms include surface albedo (α); downwelling surface shortwave radiation (SW); downwelling surface longwave radiation (LW); surface latent heat flux (LH); surface sensible heat flux (SH); and the sum of these five terms (Total). Also included is the downwelling surface solar radiation term based on clear-sky surface solar radiation (SW_{clear}) and the inferred cloudy-sky term (i.e., $SW_{cloud} = SW - SW_{clear}$), analogous clear-sky and cloudy-sky terms for LW radiation, as well as transpiration (TRANS) and evaporation (EVAP; this includes sublimation). The SEB decomposition is performed over all land areas. Also included are the corresponding land-only surface temperature (TS) and near-surface air temperature (TAS) responses. Uncertainty represents the 90% confidence interval estimated as $\frac{1.65\times\sigma}{\sqrt{m}}$, where σ is the standard deviation across models and *m* is the number of models. Responses not significant at the 90% confidence level are in bold. Units are K.

	Global		Tropics		Extratropics	
	MMM	**# Models**	**MMM**	**# Models**	**MMM**	**# Models**
α	0.11 ± 0.06	13/15	0.06 ± 0.04	11/15	0.16 ± 0.09	13/15
SW	0.09 ± 0.06	12/15	**0.05 ± 0.06**	9/15	0.16 ± 0.10	12/15
SW_{clear}	−0.05 ± 0.02	12/15	−0.05 ± 0.02	12/15	−0.05 ± 0.04	11/15
SW_{cloud}	0.14 ± 0.05	12/15	0.10 ± 0.05	11/15	0.21 ± 0.08	13/15
LW	0.20 ± 0.13	13/15	0.15 ± 0.08	13/15	0.20 ± 0.16	13/15
LW_{clear}	0.27 ± 0.13	12/14	0.22 ± 0.09	12/14	0.32 ± 0.17	12/14
LW_{cloud}	−0.07 ± 0.03	12/14	−0.07 ± 0.03	11/14	−0.11 ± 0.05	11/14
LH	0.27 ± 0.11	13/15	0.45 ± 0.15	14/15	0.19 ± 0.12	12/15
TRANS	0.45 ± 0.15	13/13	0.70 ± 0.26	13/13	0.34 ± 0.13	13/13
EVAP	−0.19 ± 0.16	9/13	−0.26 ± 0.25	7/13	−0.17 ± 0.14	12/13
SH	−0.34 ± 0.08	13/15	−0.47 ± 0.10	13/15	−0.33 ± 0.11	13/15
Total	0.33 ± 0.13	14/15	0.25 ± 0.09	13/15	0.39 ± 0.18	14/15
TS	0.26 ± 0.12	13/15	0.22 ± 0.09	13/15	0.31 ± 0.16	14/15
TAS	0.28 ± 0.13	14/15	0.25 ± 0.09	14/15	0.33 ± 0.17	14/15

Supplementary Table 5. Spatial correlations between the multimodel mean surface energy balance (SEB) terms and the total SEB term. Global, tropical and extratropical multimodel mean correaltions. Terms include surface albedo (α); downwelling surface shortwave radiation (SW); downwelling surface longwave radiation (LW); surface latent heat flux (LH); and surface sensible heat flux (SH). Also included is the downwelling surface solar radiation term based on clear-sky surface solar radiation (SW_{clear}) and the inferred cloudy-sky term (i.e., $SW_{cloud} = SW - SW_{clear}$), analogous clear-sky and cloudy-sky terms for LW radiation, as well as transpiration (TRANS) and evaporation (EVAP; this includes sublimation). All correlations are significant at the 90% confidence level.

	Global	**Tropics**	**Extratropics**
α	0.56	−0.34	0.42
SW	0.55	0.53	0.51
SW_{clear}	−0.53	−0.33	−0.41
SW_{cloud}	0.62	0.61	0.57
LW	0.63	0.37	0.58
LW_{clear}	0.91	0.76	0.90
LW_{cloud}	−0.46	−0.59	−0.50
LH	0.22	0.77	0.18
TRANS	0.23	0.55	0.32
EVAP	−0.24	−0.23	−0.39
SH	−0.36	−0.64	−0.34

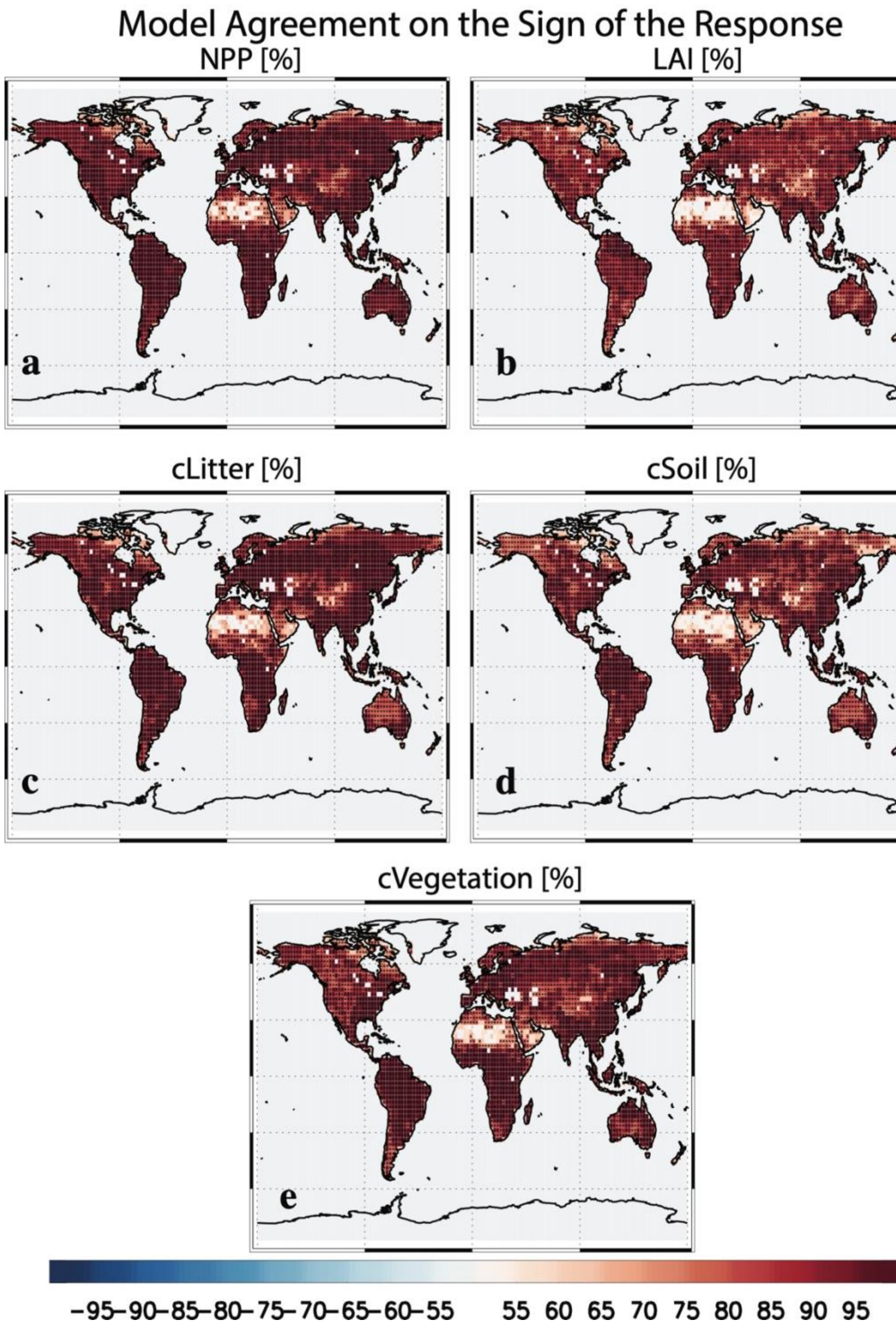

Supplementary Figure 1. Model agreement on the sign of the vegetation and land carbon responses. Model agreement on the sign of the response [% of models] for (a) net primary productivity (NPP); (b) leaf area index (LAI); (c) litter pool carbon (cLitter); (d) soil pool carbon (cSoil); and (e) vegetation carbon (cVegetation). Red (blue) colors indicate model agreement on an increase (decrease). Symbols represent significant model agreement at the 90% confidence level based on a two-tailed binomial test.

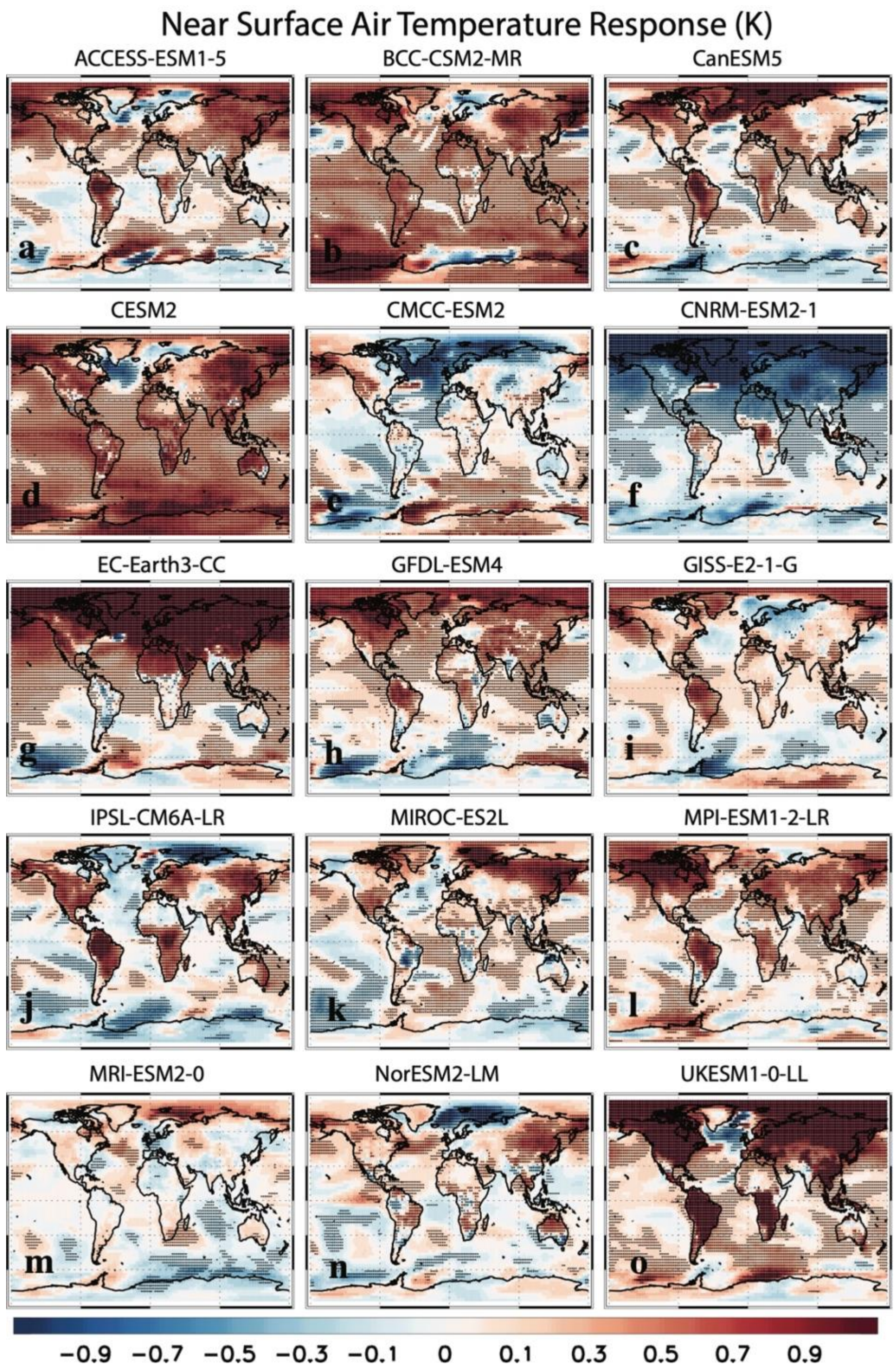

Supplementary Figure 2. Annual mean near surface air temperature response for each model. ΔTAS (K) for (a) ACCESS-ESM1-5; (b) BCC-CSM2-MR; (c) CanESM5; (d) CESM2; (e) CMCC-ESM2; (f) CNRM-ESM2-1; (g) EC-Earth3-CC; (h) GFDL-ESM4; (i) GISS-E2-1-G; (j) IPSL-CM6A-LR; (k) MIROC-ES2L; (l) MPI-ESM1-2-LR; (m) MRI-ESM2-0; (n) NorESM2-LM; (o) UKESM1-0-LL. Symbols denote a response significant at the 90% confidence level based on a two-tailed pooled t-test.

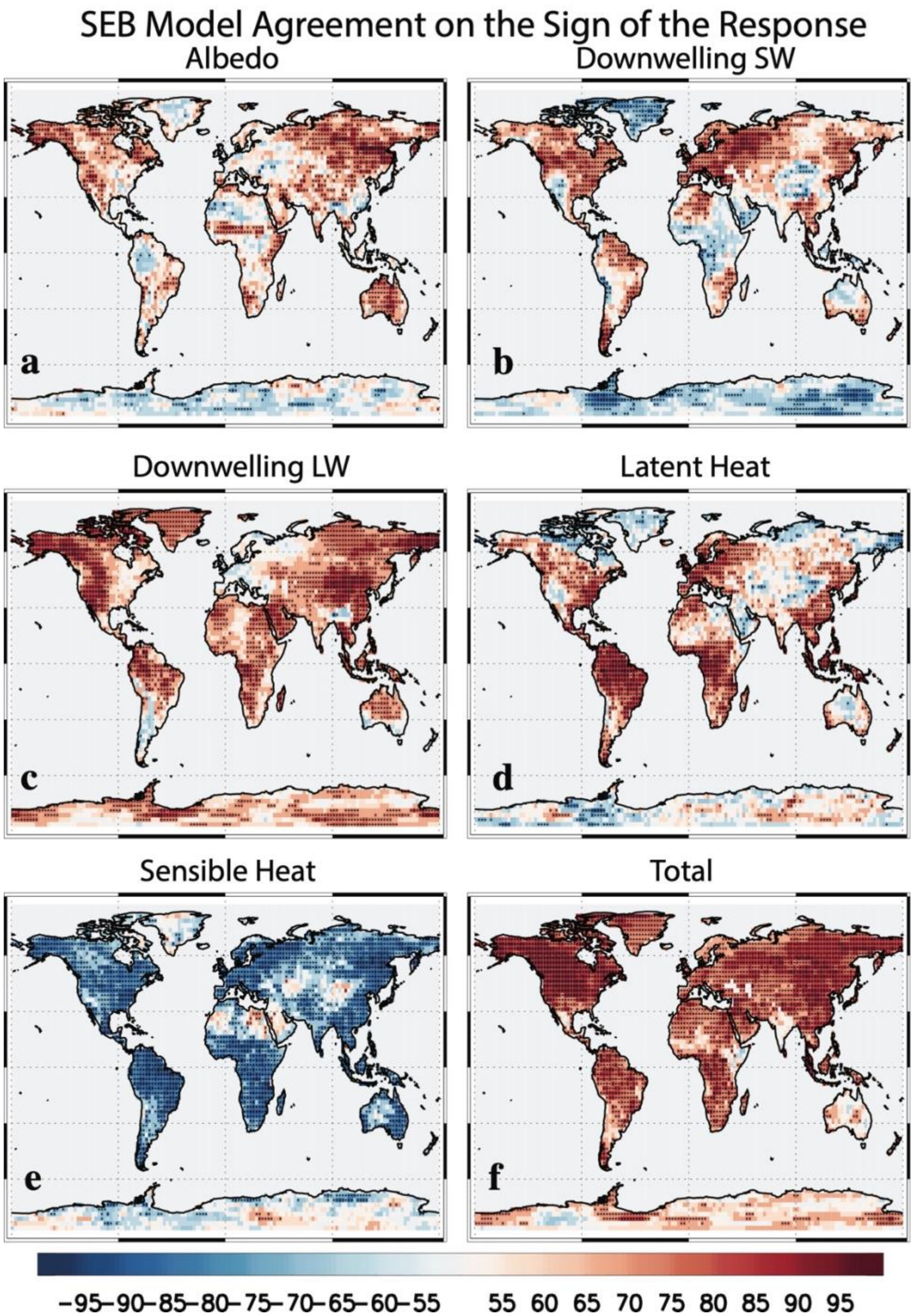

Supplementary Figure 3. Model agreement on the sign of the surface energy balance (SEB) decomposition responses. Model agreement on the sign of SEB responses [% of models] for (a) surface albedo; (b) downwelling surface shortwave radiation; (c) downwelling surface longwave radiation; (d) surface latent heat flux; (e) surface sensible heat flux; and (f) the total (i.e., sum of the prior five terms). Red (blue) colors indicate model agreement on an increase (decrease). Symbols represent significant model agreement at the 90% confidence level based on a two-tailed binomial test.

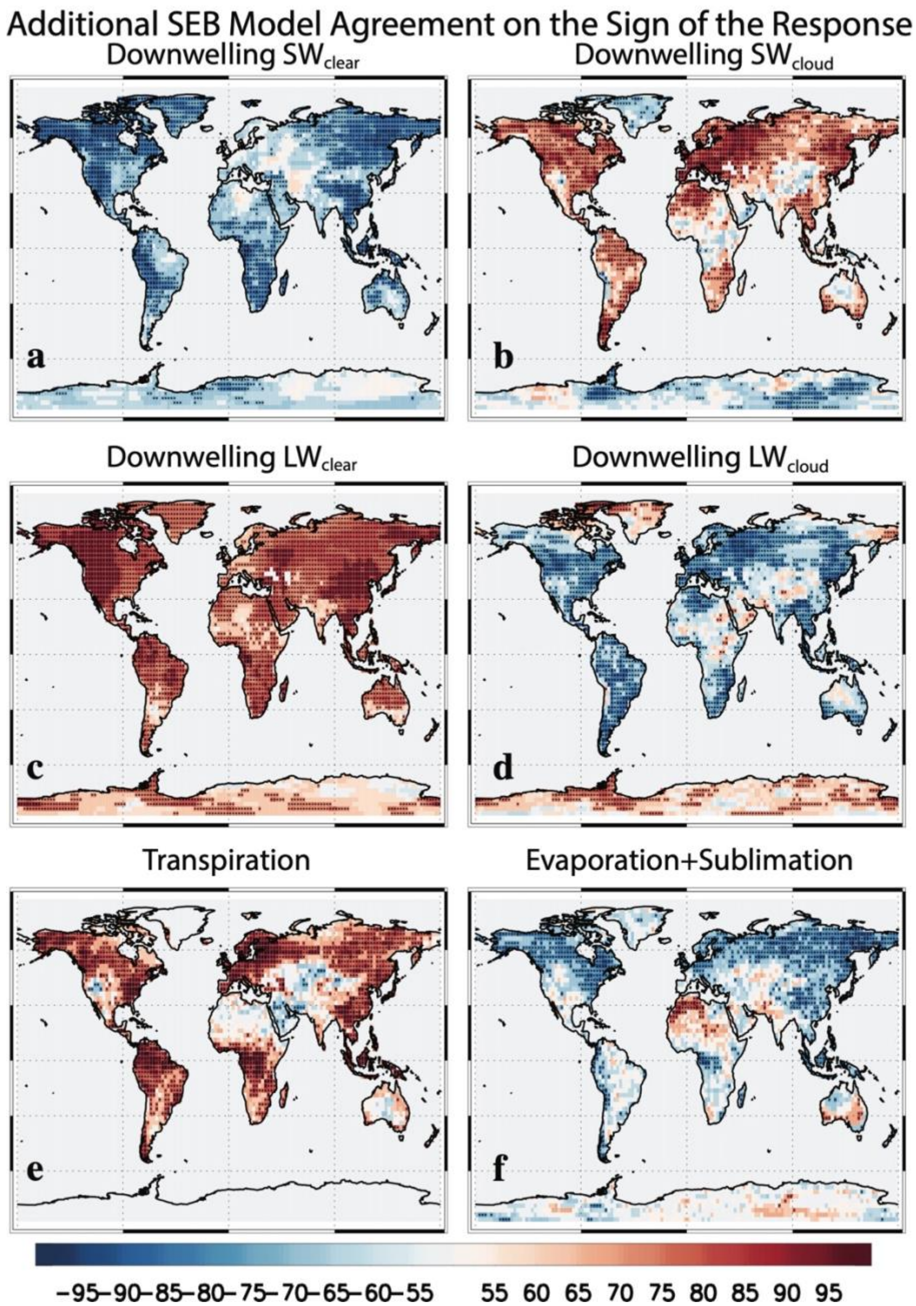

Supplementary Figure 4. Model agreement on the sign of the additional surface energy balance (SEB) decomposition responses. Model agreement on the sign of SEB responses [% of models] for downwelling surface shortwave radiation decomposed into (a) clear-sky (SW_{clear}) and (b) cloudy-sky (SW_{cloud}) contributions; downwelling surface longwave radiation decomposed into (c) clear-sky (LW_{clear}) and (d) cloudy-sky (LW_{cloud}) contributions; and surface latent heat flux decomposed into (e) canopy transpiration and (f) evaporation (which includes sublimation) contributions. Red (blue) colors indicate model agreement on an increase (decrease). Symbols represent significant model agreement at the 90% confidence level based on a two-tailed binomial test.

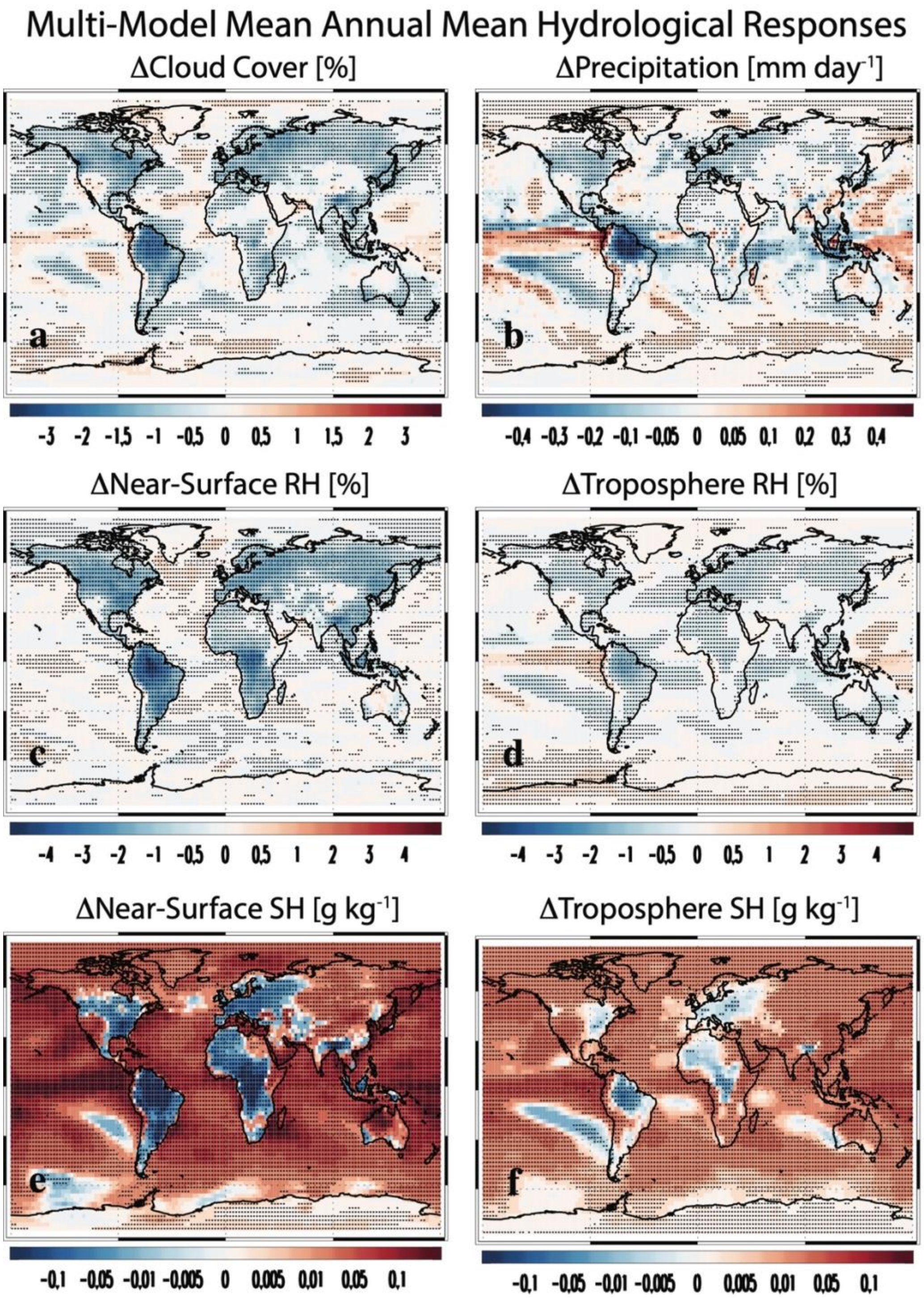

Supplementary Figure 5. Multimodel mean hydrological responses. Multimodel mean annual mean responses for (a) total cloud cover [%]; (b) precipitation [mm day^{-1}]; (c) near-surface relative humidity [%]; (d) tropospheric mean relative humidity [%]; (e) near surface specific humidity [g kg^{-1}]; and (f) tropospheric mean specific humidity [g kg^{-1}]. Symbols denote a response significant at the 90% confidence level based on a two-tailed pooled t-test.

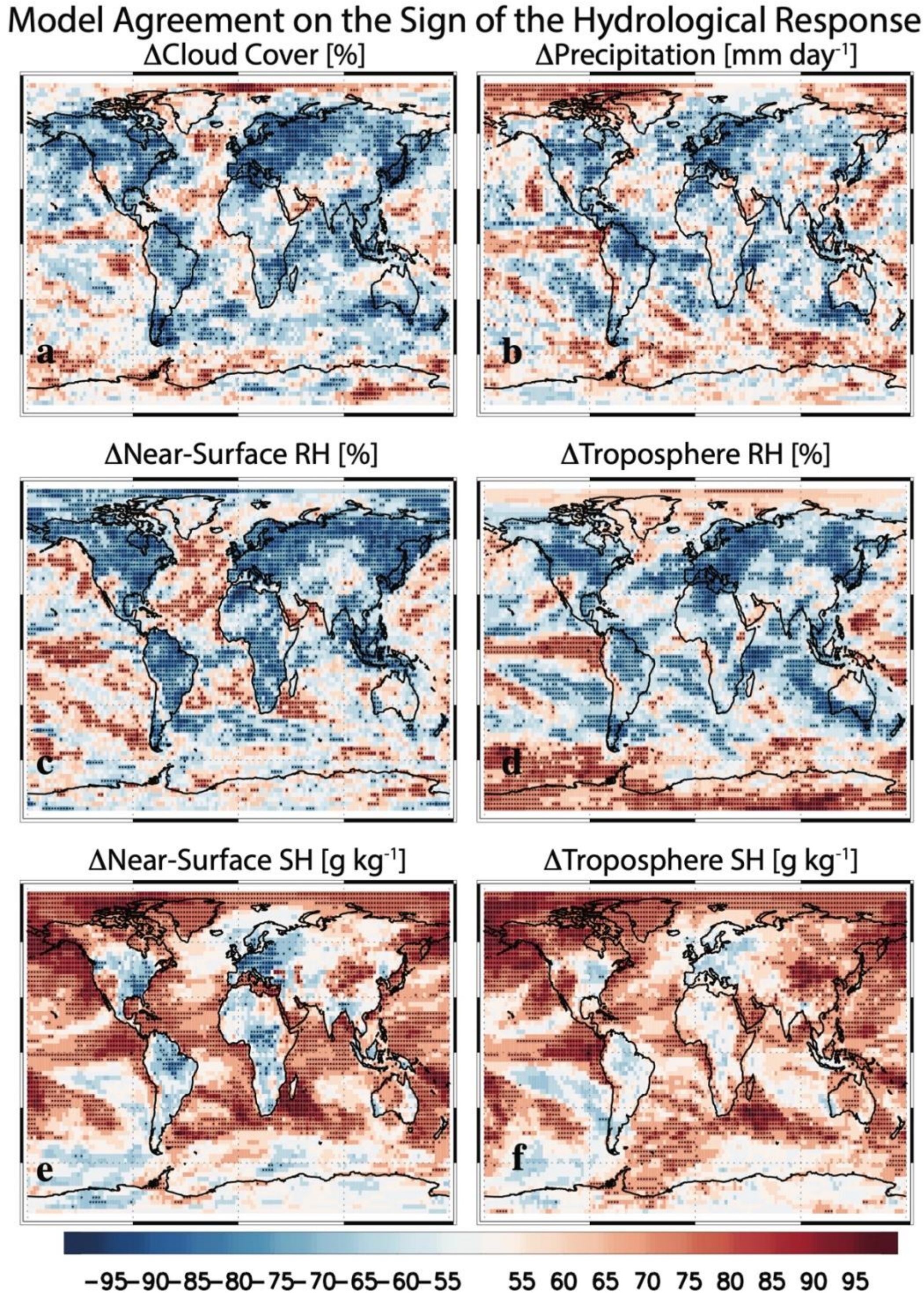

Supplementary Figure 6. Model agreement on the sign of the hydrological responses. Model agreement on the sign of hydrological responses [% of models] for (a) total cloud cover; (b) precipitation; (c) near-surface relative humidity; (d) tropospheric mean relative humidity; (e) near surface specific humidity; and (f) tropospheric mean specific humidity. Red (blue) colors indicate model agreement on an increase (decrease). Symbols represent significant model agreement at the 90% confidence level based on a two-tailed binomial test.

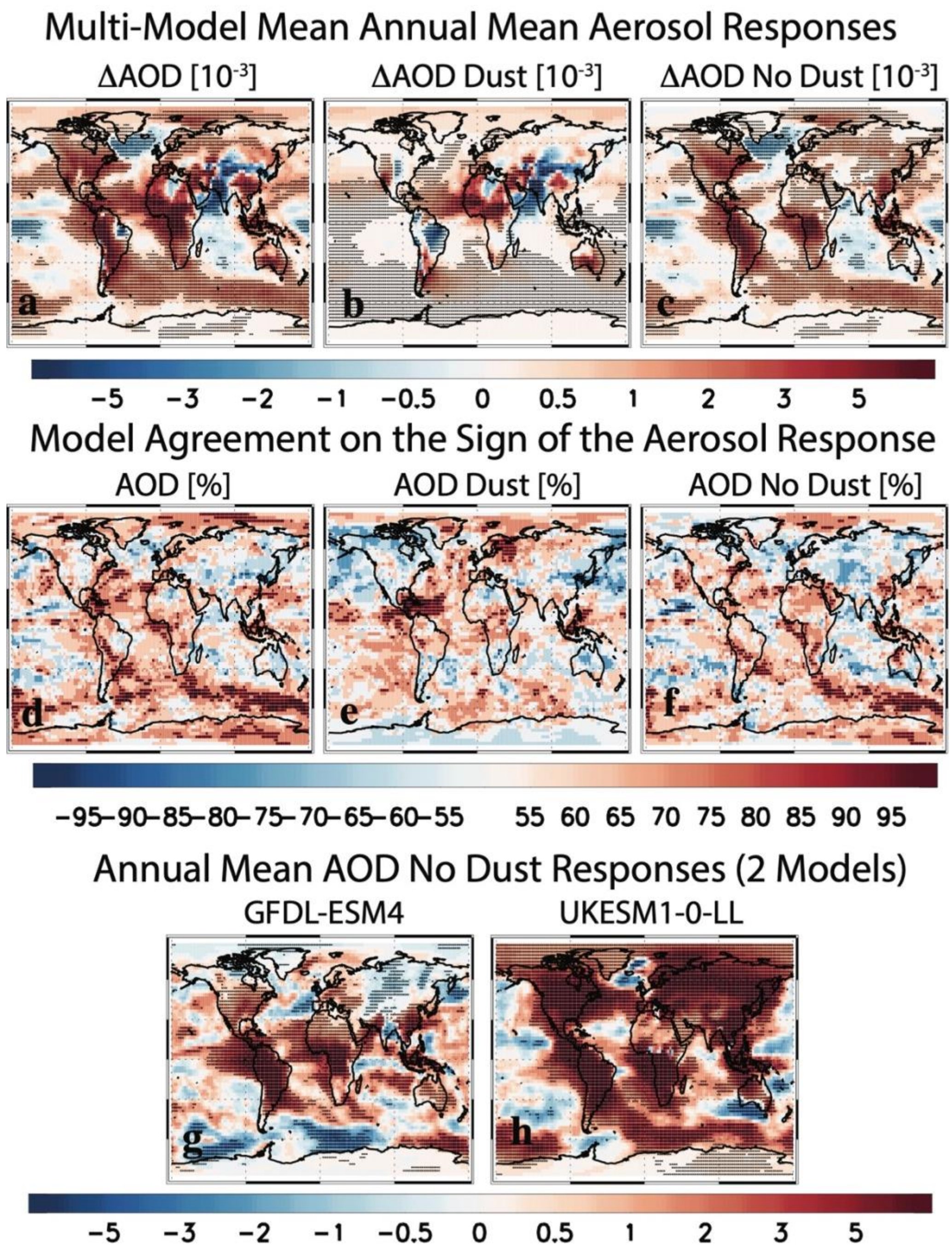

Supplementary Figure 7. Aerosol optical depth responses. Multimodel mean annual mean responses for (a) total aerosol optical depth [10^{-3}]; (b) dust aerosol optical depth [10^{-3}] and (c) aerosol optical depth without dust [10^{-3}]. Symbols denote a response significant at the 90% confidence level based on a two-tailed pooled t-test. Model agreement on the sign of aerosol responses [% of models] for (d) total aerosol optical depth; (e) dust optical depth and (f) aerosol optical depth without dust. Red (blue) colors indicate model agreement on an increase (decrease). Symbols represent significant model agreement at the 90% confidence level based on a two-tailed binomial test. Also included is the aerosol optical depth without dust response for two models with interactive chemistry and BVOCs including (g) GFDL-ESM4 and (h) UKESM1-0-LL.

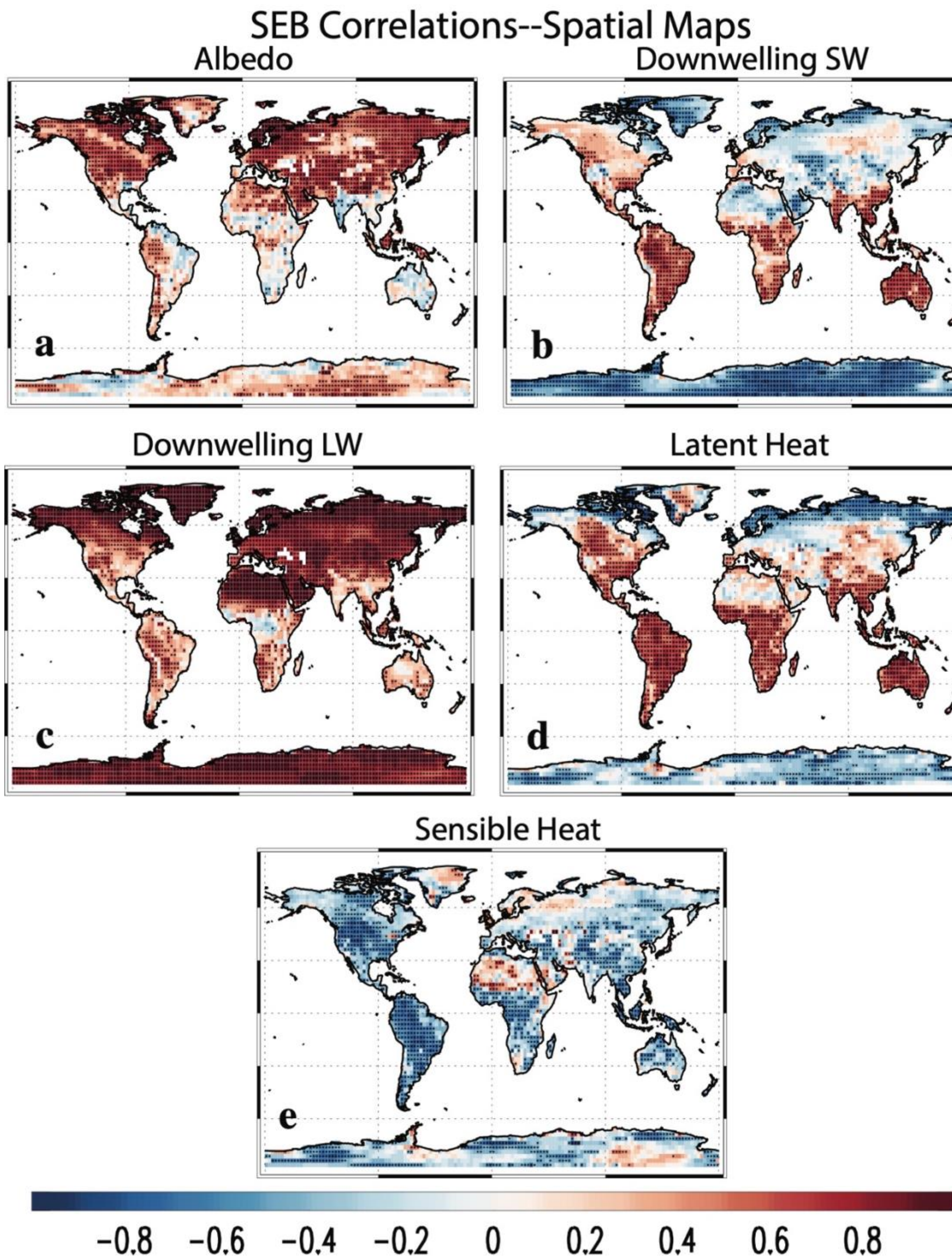

Supplementary Figure 8. Spatial correlation maps of SEB terms across models. Correlation maps between the SEB surface temperature response and the SEB surface (a) albedo; (b) downwelling SW radiation; (c) downwelling LW radiation; (d) latent heat; and (e) sensible heat response. Correlations at each grid box are across the models. Symbols denote a correlation significant at the 90% confidence level based on a two-tailed t-test.

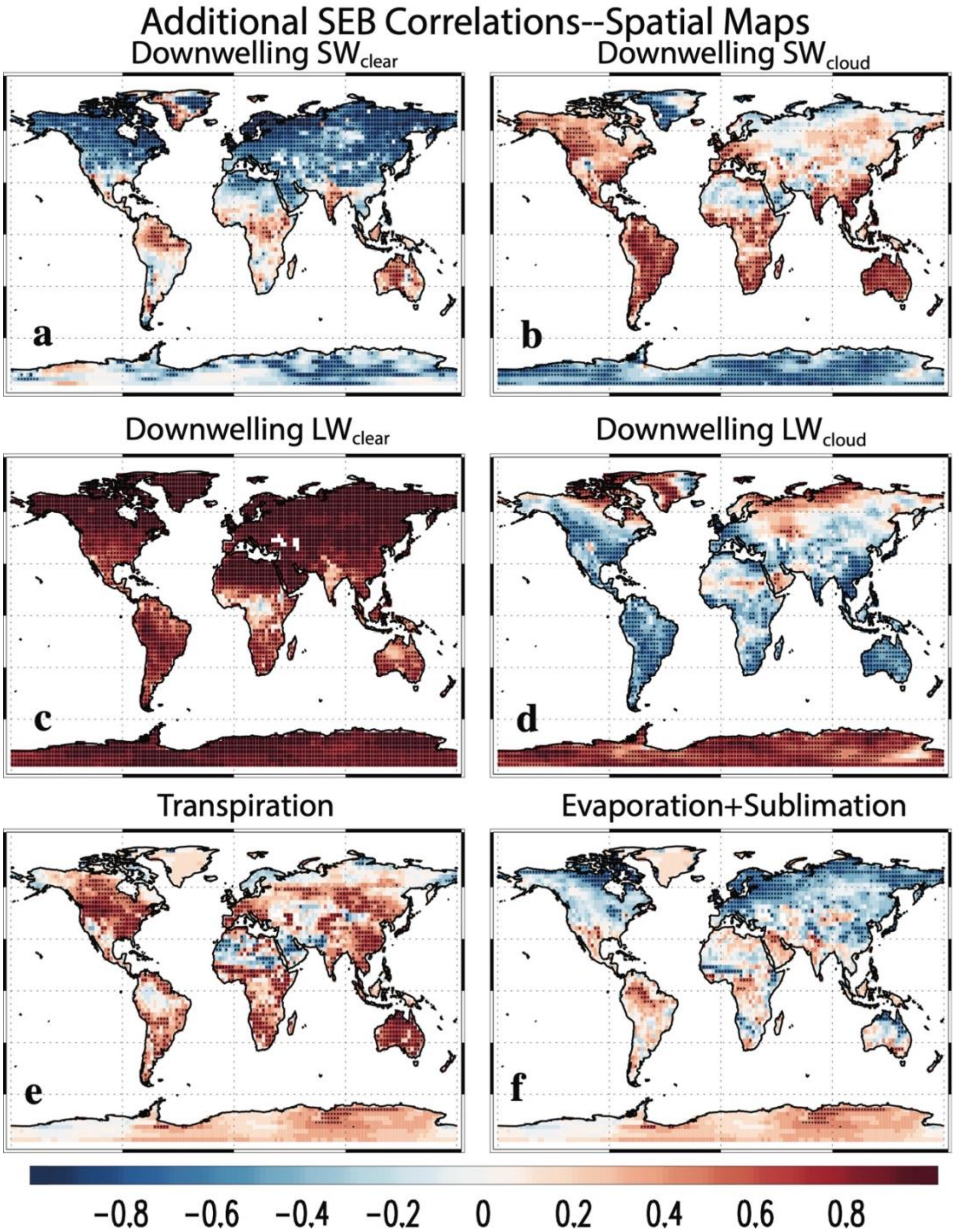

Supplementary Figure 9. Spatial correlation maps of the additional SEB terms across models. Correlation maps between the SEB surface temperature response and the SEB surface (a) downwelling SW clear-sky radiation; (b) downwelling SW cloudy-sky radiation; (c) downwelling LW clear-sky radiation; (d) downwelling LW cloudy-sky radiation; (e) transpiration and (f) evaporation (which includes sublimation) response. Correlations at each grid box are across the models. Symbols denote a correlation significant at the 90% confidence level based on a two-tailed t-test.

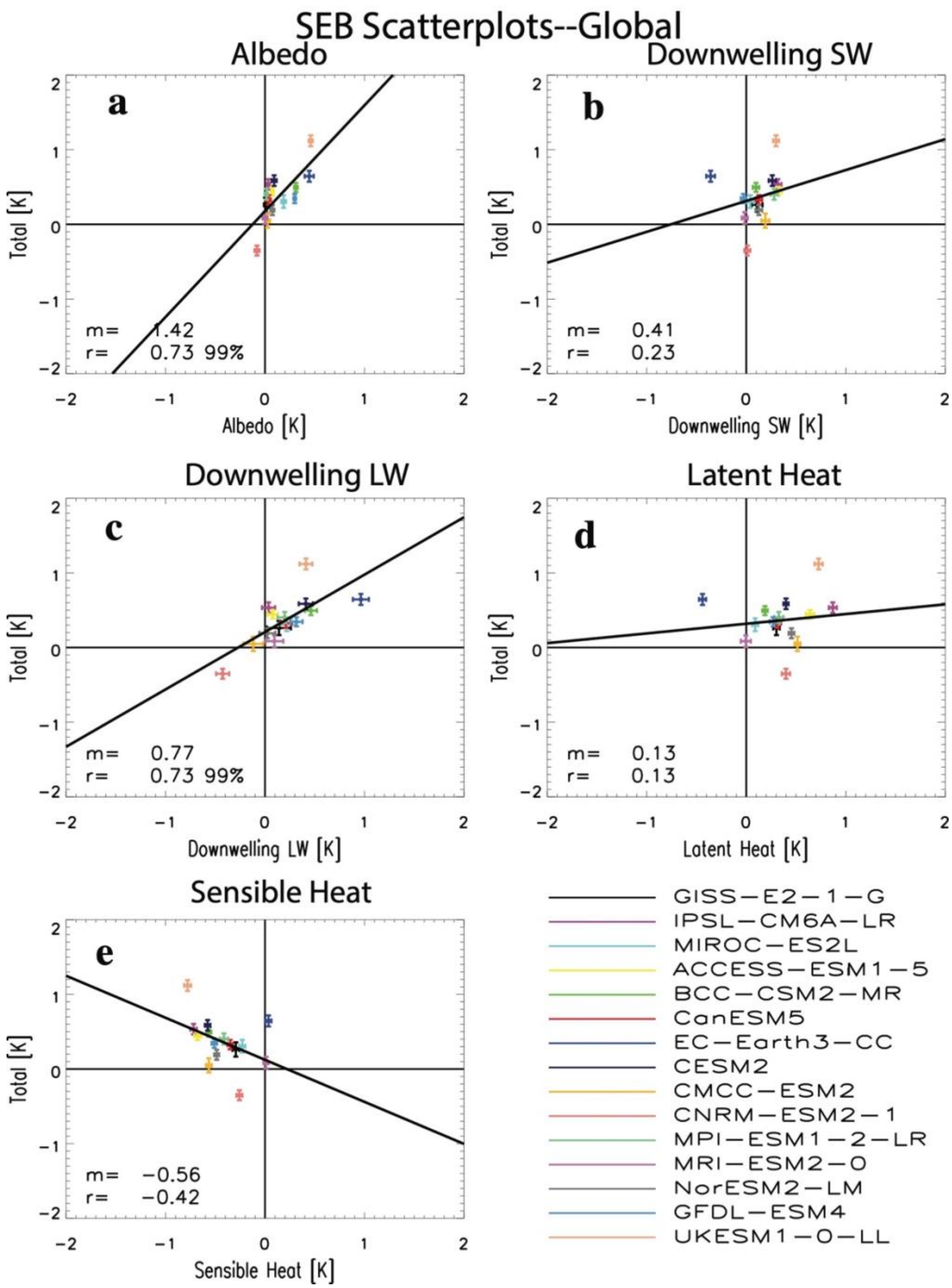

Supplementary Figure 10. Scatterplots of the global land mean SEB responses across models. Scatterplots between the global land mean SEB surface temperature response (Total, Y-axes) and the corresponding SEB surface (a) albedo; (b) downwelling SW radiation; (c) downwelling LW radiation; (d) latent heat; and (e) sensible heat response. Each symbol represents an individual model (see legend). Error bars for each symbol represent the 90% confidence intervals based on a two-tailed pooled t-test. Black line represents the least squares linear regression line. The corresponding slope (m) of the regression and the correlation coefficient (r) are included. Significant correlations based on a two-tailed test at the 90%, 95% or 99% confidence level are indicated. Units are K.

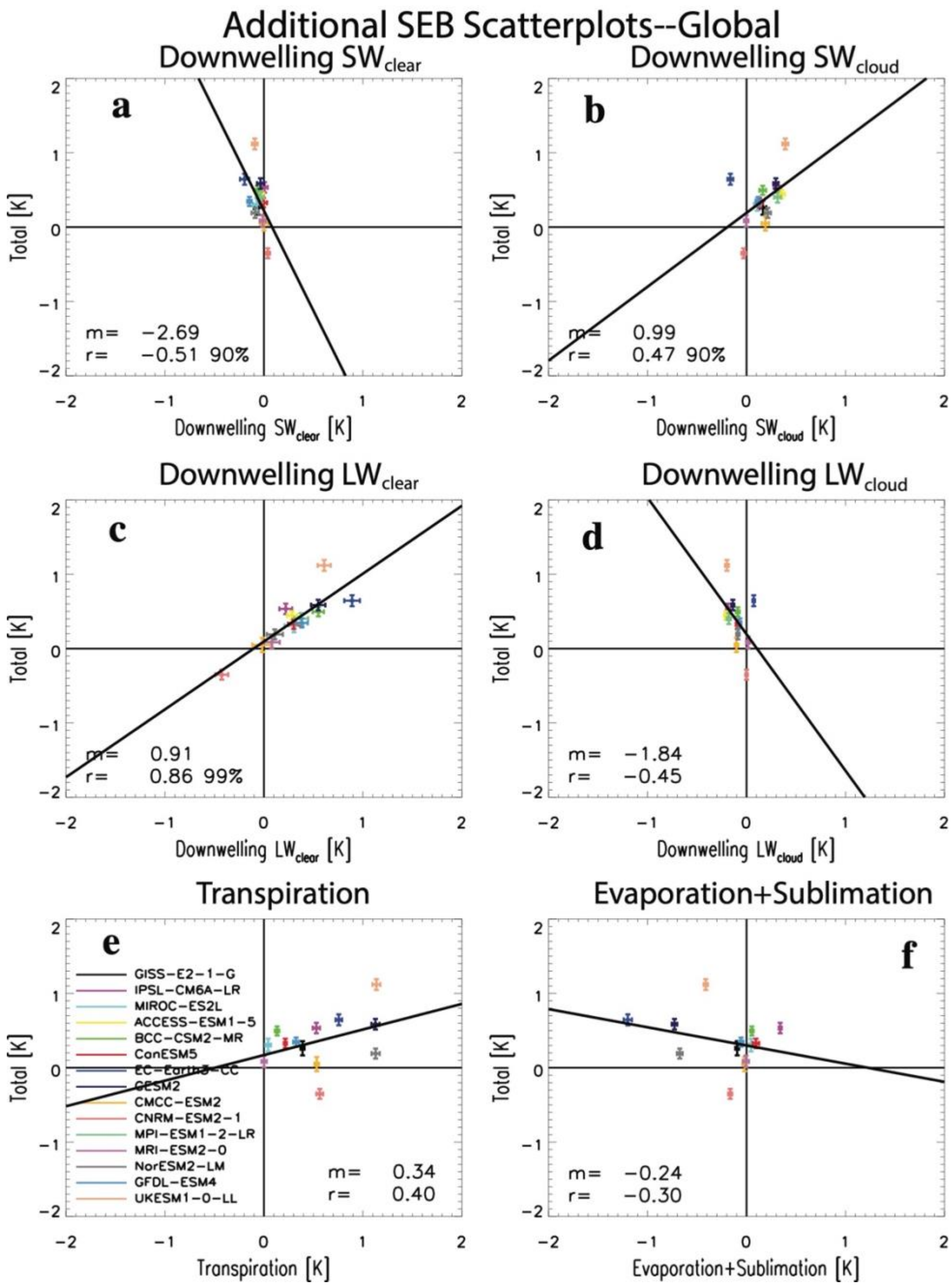

Supplementary Figure 11. Additional scatterplots of the global land mean SEB responses across models. Scatterplots between the global land mean SEB surface temperature response (Total, Y-axes) and the corresponding SEB surface (a) downwelling SW clear-sky radiation; (b) downwelling SW cloudy-sky radiation; (c) downwelling LW clear-sky radiation; (d) downwelling LW cloudy-sky radiation; (e) transpiration and (f) evaporation (which includes sublimation) response. Each symbol represents an individual model (see legend). Error bars for each symbol represent the 90% confidence intervals based on a two-tailed pooled t-test. Black line represents the least squares linear regression line. The corresponding slope (m) of the regression and the correlation coefficient (r) are included. Significant correlations based on a two-tailed test at the 90%, 95% or 99% confidence level are indicated. Units are K.

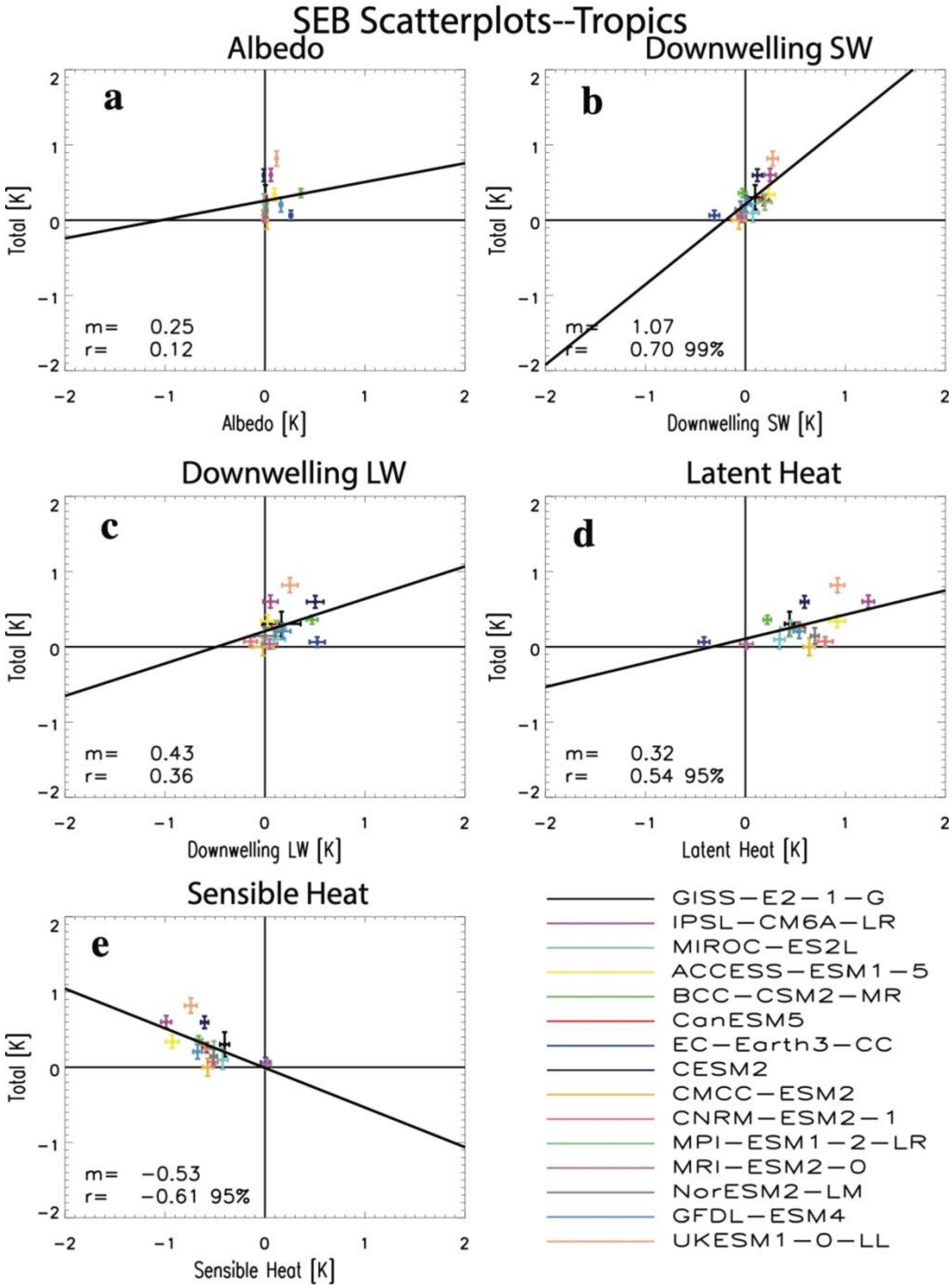

Supplementary Figure 12. Scatterplots of the tropical land mean SEB responses across models. Scatterplots between the tropical land mean SEB surface temperature response (Total, Y-axes) and the corresponding SEB surface (a) albedo; (b) downwelling SW radiation; (c) downwelling LW radiation; (d) latent heat; and (e) sensible heat response. Each symbol represents an individual model (see legend). Error bars for each symbol represent the 90% confidence intervals based on a two-tailed pooled t-test. Black line represents the least squares linear regression line. The corresponding slope (m) of the regression and the correlation coefficient (r) are included. Significant correlations based on a two-tailed test at the 90%, 95% or 99% confidence level are indicated. Units are K.

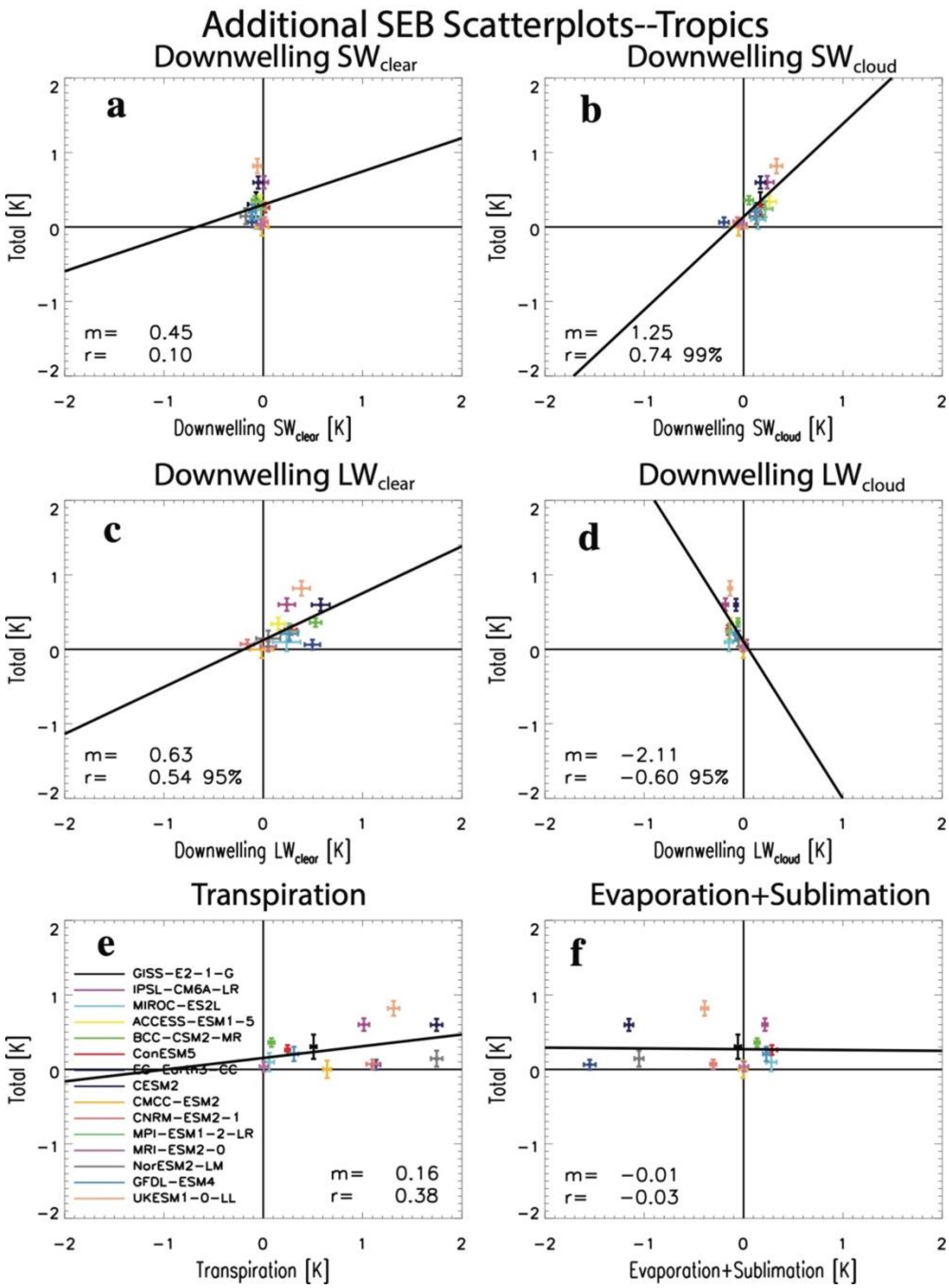

Supplementary Figure 13. Additional scatterplots of the tropical land mean SEB responses across models. Scatterplots between the tropical land mean SEB surface temperature response (Total, Y-axes) and the corresponding SEB surface (a) downwelling SW clear-sky radiation; (b) downwelling SW cloudy-sky radiation; (c) downwelling LW clear-sky radiation; (d) downwelling LW cloudy-sky radiation; (e) transpiration and (f) evaporation (which includes sublimation) response. Each symbol represents an individual model (see legend). Error bars for each symbol represent the 90% confidence intervals based on a two-tailed pooled t-test. Black line represents the least squares linear regression line. The corresponding slope (m) of the regression and the correlation coefficient (r) are included. Significant correlations based on a two-tailed test at the 90%, 95% or 99% confidence level are indicated. Units are K.

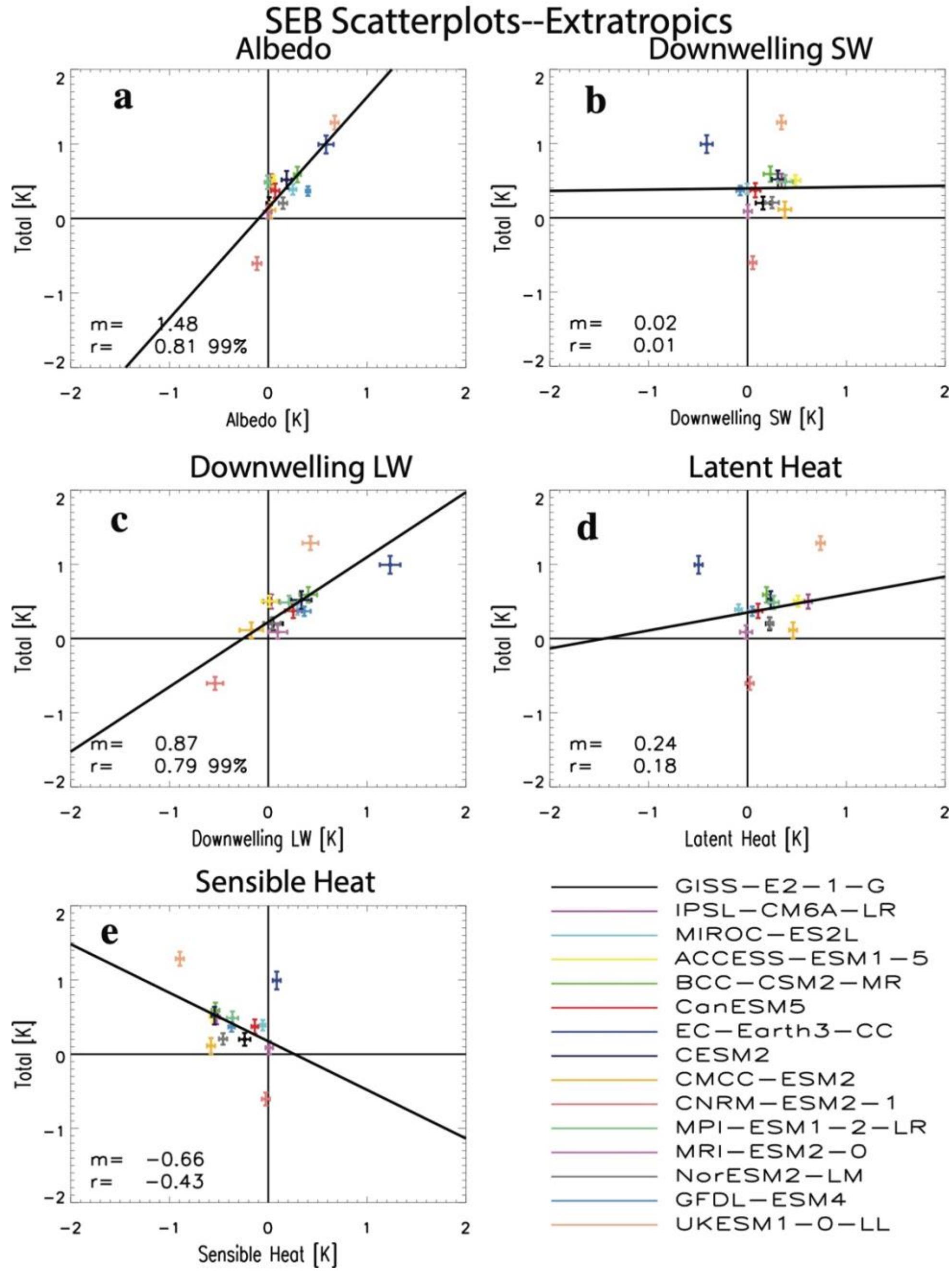

Supplementary Figure 14. Scatterplots of the extratropical land mean SEB responses across models. Scatterplots between the extratropical land mean SEB surface temperature response (Total, Y-axes) and the corresponding SEB surface (a) albedo; (b) downwelling SW radiation; (c) downwelling LW radiation; (d) latent heat; and (e) sensible heat response. Each symbol represents an individual model (see legend). Error bars for each symbol represent the 90% confidence intervals based on a two-tailed pooled t-test. Black line represents the least squares linear regression line. The corresponding slope (m) of the regression and the correlation coefficient (r) are included. Significant correlations based on a two-tailed test at the 90%, 95% or 99% confidence level are indicated. Units are K.

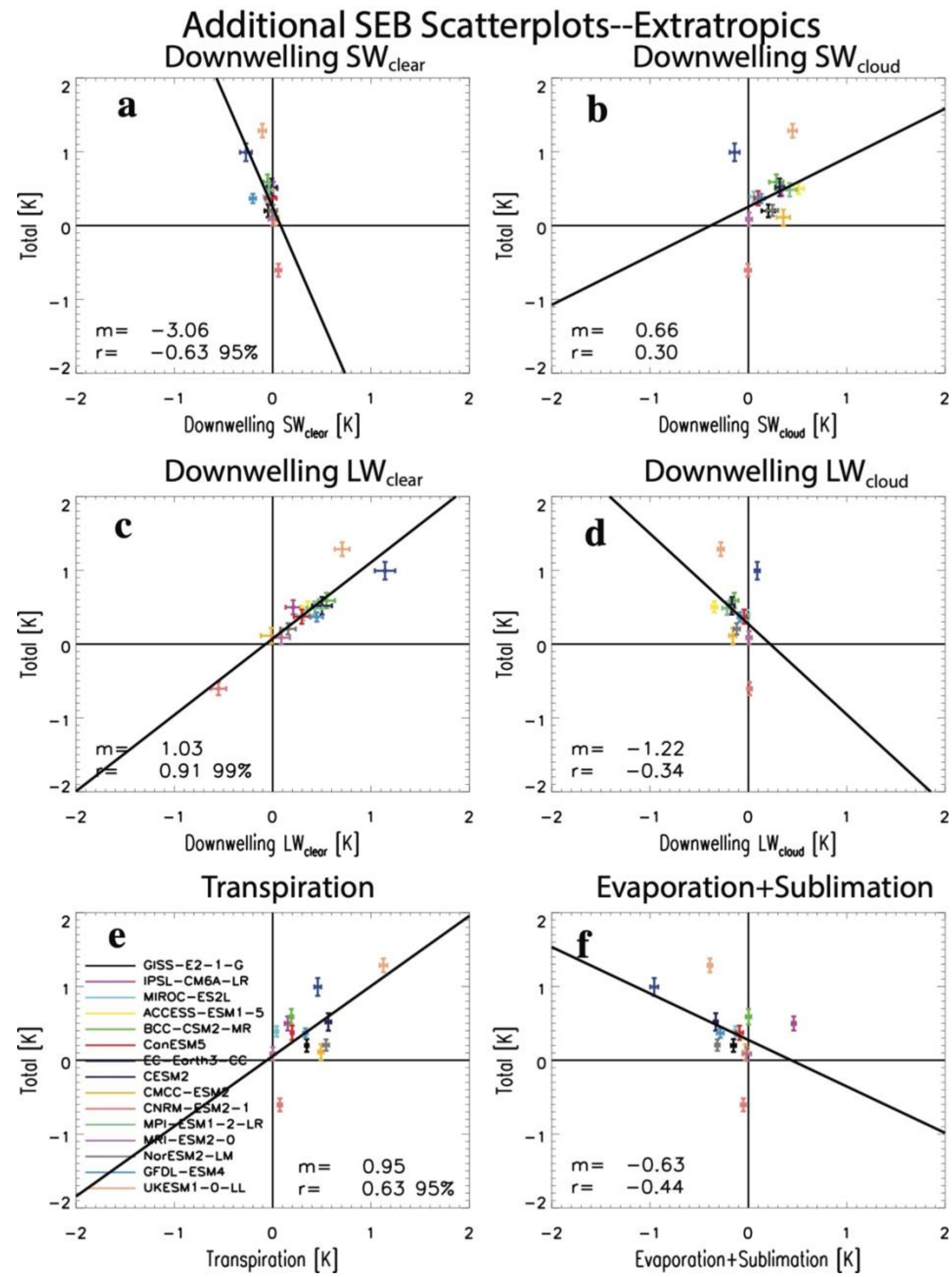

Supplementary Figure 15. Additional scatterplots of the extratropical land mean SEB responses across models. Scatterplots between the extratropical land mean SEB surface temperature response (Total, Y-axes) and the corresponding SEB surface (a) downwelling SW clear-sky radiation; (b) downwelling SW cloudy-sky radiation; (c) downwelling LW clear-sky radiation; (d) downwelling LW cloudy-sky radiation; (e) transpiration and (f) evaporation (which includes sublimation) response. Each symbol represents an individual model (see legend). Error bars for each symbol represent the 90% confidence intervals based on a two-tailed pooled t-test. Black line represents the least squares linear regression line. The corresponding slope (m) of the regression and the correlation coefficient (r) are included. Significant correlations based on a two-tailed test at the 90%, 95% or 99% confidence level are indicated. Units are K.